frontiers | Frontiers in Chemistry

TYPE Original Research
PUBLISHED 24 October 2024
DOI 10.3389/fchem.2024.1482006

OPEN ACCESS

EDITED BY
Shu Wang,
Harbin University of Science and Technology, China

REVIEWED BY
Liu Xuefei,
Guizhou Normal University, China
Guangzhao Wang,
Yangtze Normal University, China

*CORRESPONDENCE
Qingyun Sun,
sunqingyun@njfu.edu.cn
Weihua Mu,
muwh@ucas.ac.cn
Zhen Cui,
zcui@xaut.edu.cn

RECEIVED 17 August 2024
ACCEPTED 16 September 2024
PUBLISHED 24 October 2024

CITATION
Xu P, Zhu Z, Zheng R, Sun Q, Ma Z, Mu W and Cui Z (2024) Predicting the characteristics of a C_2B_6 monolayer with ultrahigh carrier mobility. *Front. Chem.* 12:1482006.
doi: 10.3389/fchem.2024.1482006

Predicting the characteristics of a C_2B_6 monolayer with ultrahigh carrier mobility

Ping Xu[1], Zhengyang Zhu[2], Ruxin Zheng[3], Qingyun Sun[4,5]*, Zhen Ma[6], Weihua Mu[7]* and Zhen Cui[8]*

[1]Jiangsu Vocational College of Agriculture and Forestry, Jiangsu, China, [2]School of Mechanical Engineering, Wanjiang University of Technology, Maanshan, China, [3]School of Mechanical Engineering, Southeast University, Nanjing, China, [4]School of Mechanical and Electronic Engineering, Nanjing Forestry University, Nanjing, Jiangsu, China, [5]Nanjing Boya Intelligent Technology Co., Ltd, Jiangsu, China, [6]School of Agricultural Engineering, Jiangsu University, Zhenjiang, China, [7]Wenzhou Institute, University of Chinese Academy of Sciences, Wenzhou, China, [8]School of Automation and Information Engineering, Xi'an University of Technology, Xi'an, China

Two-dimensional materials have excellent electronic and optical properties, suggesting absolute advantages in nanodevices. In this work, a new two-dimensional material with a puckered structure, a C_2B_6 monolayer, is proposed. The material presents dynamic and thermal stability calculated by first-principle simulations. Interestingly, the C_2B_6 monolayer possesses semiconductor behavior with an ultra-narrow bandgap of approximately 0.671 eV by HSE06 functional. Meanwhile, the hole in the C_2B_6 monolayer shows ultrahigh mobility at approximately 6,342 $cm^2 \cdot V^{-1} \cdot s^{-1}$ in decent transport directions, which is larger than traditional transition metal dichalcogenides materials. More importantly, the pronounced anisotropy of mobility of the electrons and holes can separate the photogenerated charges, suggesting the applications for photocatalytic, photovoltaic and optical and cold chain electronic devices. Then, the novel properties of the light absorption characteristic are obtained, and the anisotropic photocurrent implies the C_2B_6 monolayer can be used as a potential photoelectric device. Our results provide theoretical guidance for the design and application of two-dimensional materials.

KEYWORDS

two-dimensional, first principle calculations, C2B6, mobility, optoelectronics

Introduction

Since the discovery of graphene (Geim and Novoselov, 2007), there has been an increasing amount of research on two-dimensional (2D) materials (Miro et al., 2014; Ren et al., 2024). The wide application of the unique properties and advantages of 2D materials has made them highly regarded research in the field of materials science (Tang et al., 2022; Wang et al., 2023; Su et al., 2022; Su et al., 2023; Sun et al., 2022). For example, due to the extremely thin thickness of transition metal dichalcogenides (TMDs), their light absorption performance is outstanding, suggesting potential applications in fields such as solar cells and optoelectronic devices (Zhao et al., 2024; Ren et al., 2019). The AlN monolayer also has outstanding strength and stiffness in the plane direction compared with the bulk one (Ren et al., 2021a; Ren et al., 2021b). In addition, the larger specific surface area exposes more catalytic active sites; therefore, 2D materials present excellent photocatalytic and electrocatalytic properties.

Wu et al. (2020) prepared IrPdPtRhRu high-entropy alloy (HEA) nanoparticles with a mean diameter of 5.5 ± 1.2 nm by a facile one-pot polyol method, which possesses a lattice constant of 3.856 Å. The HAADF-STEM configurations of the IrPdPtRhRu HEAs and the corresponding energy-dispersive X-ray (EDX) images of each element suggest the solid-solution alloys obtained by homogeneous distribution. The duration of the IrPdPtRhRu was evaluated in both acidic (0.05 M H_2SO_4) and alkaline (1.0 M KOH) electrolytes, which proves the hydrogen evolution reaction (HER) ability of the IrPdPtRhRu HEA NPs.

High throughput computing method investigations are conducted to develop new 2D materials, expand their application, and develop more novel mechanical, optical, and electronic properties (Ren et al., 2022a; Sun and Schwingenschlögl, 2021; Haastrup et al., 2018). For example, Luo used particle swarm optimization to structure boron carbon compounds, and the results show that boron carbon compounds have strong B–C bonds and thermal stability and can maintain structural stability even above 2,000 K (Luo et al., 2011). Lu proposed a CaP_3 monolayer with a direct bandgap of approximately 1.15 eV, and the electron mobility obtained is as high as 19,930 $cm^2 \cdot V^{-1} \cdot s^{-1}$ (Lu et al., 2018). Yuan predicted the monolayered penta-RuS_4 through first-principle calculations, and interestingly, this monolayered penta-RuS_4 structure exhibits unique anisotropic secondary energy dispersion (Yuan et al., 2017). Jing presented a monolayered GeP_3 crystal that has an indirect bandgap of 0.55 eV. The double-layer GeP_3 possesses a decreased bandgap of 0.43 eV. It is noteworthy that the GeP_3 monolayer can transform the indirect bandgap into the direct bandgap under the condition of biaxial strain. Meanwhile, GeP_3 also has remarkable light absorption ability and can be widely used in optoelectronics (Jing et al., 2017).

Jin proposed a novel Janus MoTe monolayer using density functional theory (DFT). The results indicate that the monolayered Janus MoTe presents relatively wide spatial extension and low binding energy. Furthermore, the time for electron–hole recombination is approximately 1.31 ns, making it a potential photocatalyst for water splitting (Jin et al., 2018). More recently, researchers used the B_2P_6 present Janus structure and proved that B_2P_6 is an indirect bandgap semiconductor with an excellent hydrogen production efficiency of 28.2% and an outstanding photocatalyst (Sun and Schwingenschlögl, 2020a) that also can be tuned by external strain (Ren et al., 2021c). For a B_2P_6 monolayer, the HER and oxygen evolution reactions (OERs) can be induced respectively at different surfaces because the energy levels of the two surfaces exhibit staggered band energy, thereby separating the photogenerated electrons and holes. Such a Janus structure of the B_2P_6 monolayer exhibits intrinsic differences by atomic adsorption on different surfaces (Ren et al., 2022b).

A CS monolayer was proposed with strong absorption of solar radiation and conversion efficiencies as high as 20.1% (Sun and Schwingenschlögl, 2020b), which also presents decent band edge positions for the redox reaction in water splitting used as a photocatalyst. A CN monolayer shows a wide bandgap of approximately 6 eV as a potential power device (Ren et al., 2023a). The wide bandgap and extremely strong elastic modulus of the CN monolayer enable it to maintain the potential for photocatalytic water splitting even under large strains. Thus, B- or C-atom-based new materials are proposed to possess novel electronic and optical performances for use in nanodevices.

In this investigation, a novel monolayered C_2B_6 system is proposed by the elemental mutation method considering the prototype of the Li_xB_y structure. Using the first-principle calculations, the C_2B_6 monolayer possesses excellent stability by phonon spectrum and *ab initio* molecular dynamics (AIMD) calculations. Then, the electronic feature is investigated by band structure and carrier mobility. The optical performance of the C_2B_6 monolayer is addressed by light absorption spectrum and photocurrent testing.

Computing method

All first-principle simulations were performed using the Vienna *ab initio* simulation package (VASP) (Oganov and Glass, 2006) using the DFT (Grimme et al., 2010; Van de Walle and Martin, 1989; Grest et al., 1981). The projector augmented wave potentials (PAW) were used in the calculations to demonstrate the core electrons (Kresse and Furthmüller, 1996a; Kresse and Furthmüller, 1996b; Blöchl, 1994). The Perdew–Burke–Ernzerhof (PBE) functional was conducted by the generalized gradient approximation (GGA) method (Kresse and Joubert, 1999; Perdew et al., 1996). The Heyd–Scuseria–Ernzerhof hybrid functional was explored to calculate a more accurate band structure and light absorption spectrum (Heyd et al., 2005; Heyd et al., 2003). The spin effect is not explored in the calculations because it has almost no effect on the electronic properties of the studied system, which is proved by the band structure demonstrated in Supplementary Figure S1 in Supporting Information. The energy cut-off was 550 eV. The Monkhorst–Pack *k*-point grid was set as 17 × 17 × 1 in the first Brillouin zone. The density functional perturbation theory (DFPT) was considered to obtain the phonon spectra by the PHONOPY code (Togo and Tanaka, 2015; Togo et al., 2008). Furthermore, the convergence for force was set as 0.01 eV $Å^{-1}$, while the energy of the calculated system is set as 0.01 meV. The photocurrent of the C_2B_6 monolayer is calculated by Nanodcal software based on non-equilibrium Green's function (NEGF) theory.

Results and discussion

First, the crystal structure of the C_2B_6 monolayer is predicted as a puckered unit-cell with the space group of Pca_{21}, using the elemental mutation method from the prototype of the Li_xB_y structure (Ren et al., 2022c), shown in Figure 1A. The optimized lattice parameters of the *x* and *y* in unit-cell of the C_2B_6 monolayer are 5.218 Å and 3.310 Å, respectively, which is comparable with the CS monolayer (Lv et al., 2020). The C–B bond and the C–C bonds are obtained as 1.59 Å and 1.32 Å, respectively.

The simulated STM configuration of the C_2B_6 monolayer is demonstrated in Figure 1B, which can provide a reference for experimental observations. The cohesive energy of the C_2B_6 monolayer is calculated as 6.516 eV/atom, which is obtained by $(2E_C + 6E_B - E_{CB})/8$, where E_C, E_B, and E_{CB} are the total energies of a C atom, a B atom, and the C_2B_6 monolayer, respectively. The calculated cohesive energy of the C_2B_6 monolayer is comparable with the predicted Li_xB_y system (approximately 4.11–5.53 eV/atom) (Ren et al., 2022c) and the CB monolayer (approximately 6.13 eV/atom) (Ren

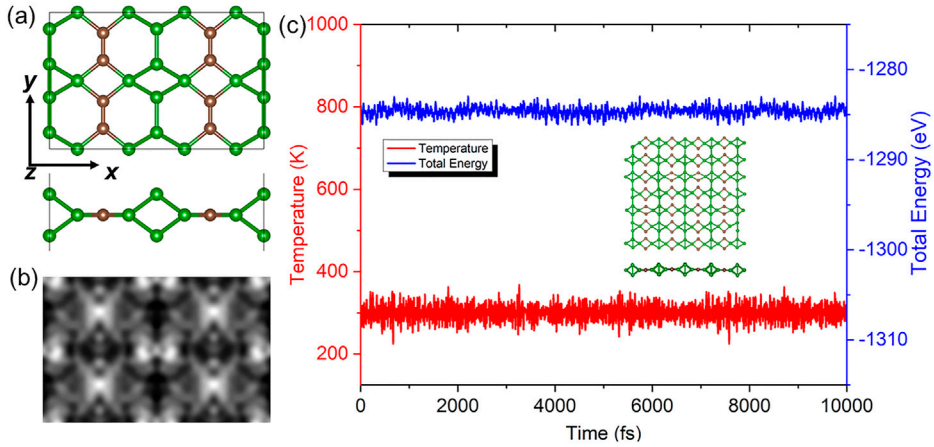

FIGURE 1
(A) Atomic structure and the **(B)** simulated STM configuration of the C_2B_6 monolayer at a voltage of −2 V. **(C)** Energy and the temperature of the C_2B_6 monolayer in the AIMD calculations. The inset is the relaxed structure of the C_2B_6 monolayer at 300 K for 10 ps. The green and the brown balls are B and C atoms, respectively.

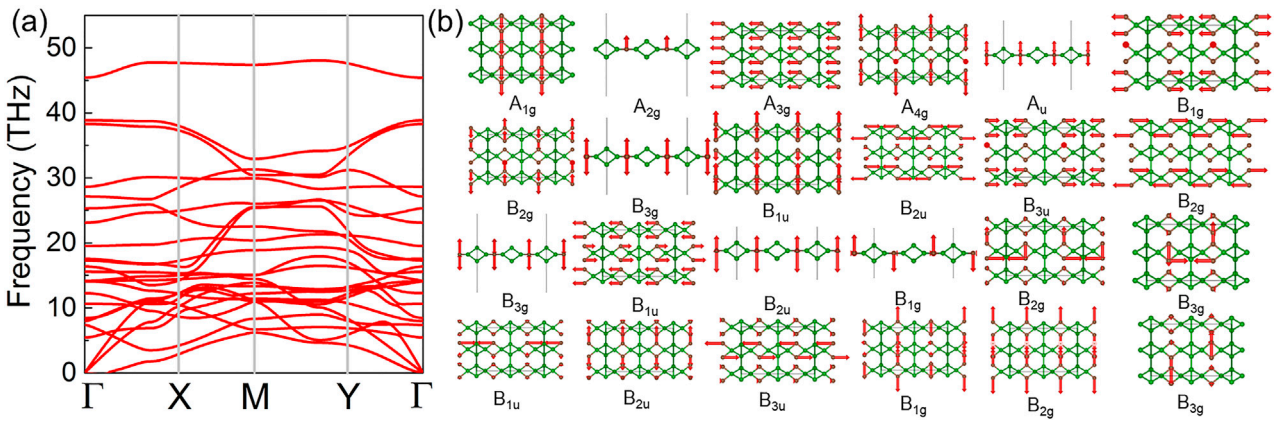

FIGURE 2
Calculated **(A)** phonon spectrum and the **(B)** atomic vibration mode of the C_2B_6 monolayer.

et al., 2023a). It is also larger than that of the V–VI system (approximately 3.37–3.81 eV/atom) (Ren et al., 2022a), suggesting the stability of the C_2B_6 monolayer. The thermal stability of the C_2B_6 monolayer is estimated by the AIMD calculations using the Nosé–Hoover heat bath scheme (Nosé, 1984). The supercell of the C_2B_6 monolayer is constructed on a $7 \times 4 \times 1$ grid to ensure the lattice translational constraints contain 192 atoms (Ren et al., 2020a). The C_2B_6 monolayer is relaxed at 300 K within 10 ps. After the completed simulations, the atomic structure of the C_2B_6 monolayer is still unscathed, as shown in the insets of Figure 1C. The temperature and energy of the AIMD for the C_2B_6 monolayer are also convergent, as shown in Figure 1C, which further provides evidence of stability. The C_2B_6 monolayer is also stable under 600 K, while the structure can be melted down at the temperature of 1,000 K, as demonstrated in the Supplementary Figures S2A, B, respectively.

The dynamic stability of the C_2B_6 monolayer is investigated by phonon spectra, calculated in Figure 2A. One can see that there is no imaginary frequency in the phonon spectra of the C_2B_6 monolayer, implying the dynamic stability of the C_2B_6 system. The highest frequency of the optical branch can reach 45 THz, as shown in Figure 2A. Such maximal optical branch frequency is also comparable with the prototype (Li_xB_y system), suggesting applications as efficient thermoelectric functional devices that can be tuned by the phononic crystal structure (Ren et al., 2020b). There are 24 degeneracy points at the Γ point. The lattice vibration mode of the C_2B_6 system at the Γ point for these 24 degeneracy configurations is studied, as shown in Figure 2B. All these optical phonons at the Γ point can be demonstrated as Equation 1:

$$\Gamma_{optic} = 4A_g\ (R) + A_u\ (R) + 3B_{1g}\ (IR) + 3B_{1u}\ (R) + 2B_{2g}\ (R) + 3B_{2u}\ (IR) + B_{3g}\ (IR) + 2B_{3u}\ (R), \quad (1)$$

where R, IR, and IN represent the optical phonon mode with Raman active, infrared active, and inactive, respectively. Interestingly, A_{2g}, A_u, B_{3g}, A_{2u}, and B_{1g} are out-of-plane vibration modes, and the others are a combined form.

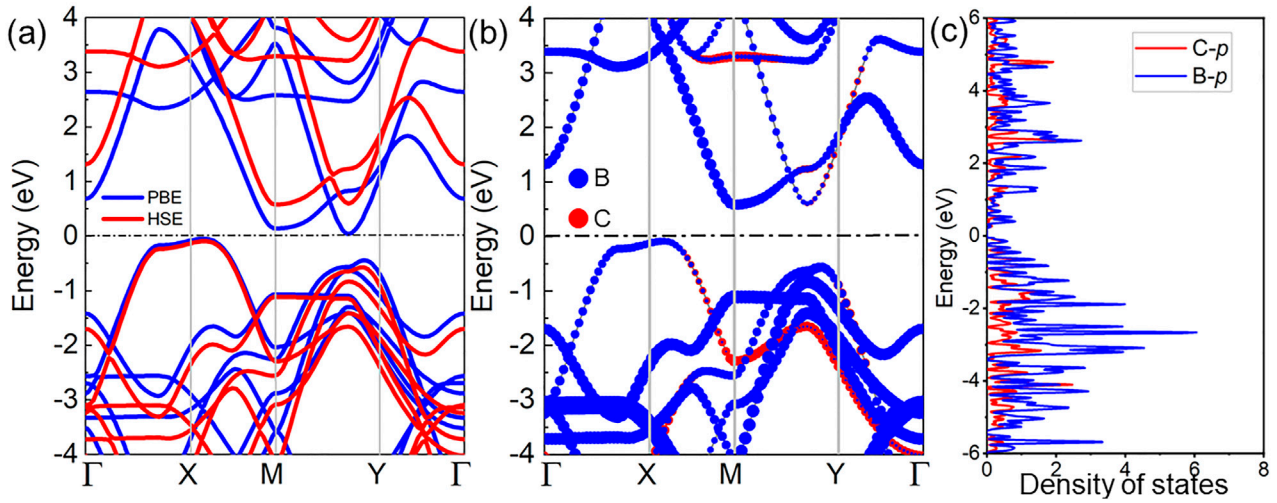

FIGURE 3
Obtained **(A)** band structure, **(B)** HSE06 calculated projected band structure, and **(C)** density of states of the C_2B_6 monolayer.

Then, the band structure of the C_2B_6 monolayer is investigated, as shown in Figure 3, by PBE and HSE06 methods. The C_2B_6 monolayer is a semiconductor with an indirect bandgap with the conduction band minimum (CBM) located between the M and Y points, while the valence band maximum (VBM) is set between the X and M points, demonstrated in Figure 3A. More interestingly, even though the wider bandgap is obtained by the HSE06 functional, it still presents as small as 0.671 eV, smaller than the As_2X_3 system (Zhao et al., 2023). It is worth noting that the ultra-narrow bandgap is also reported in the PbN/CdO heterostructure (approximately 0.128 eV). Such an ultra-narrow bandgap in the C_2B_6 monolayer facilitates rapid charge transitions and can serve as a potential efficient nanoelectronic device, optical device, and catalyst (Wang et al., 2017; Huang et al., 2024). The projected band structure of the C_2B_6 monolayer is calculated by the HSE06 in Figure 3B. The B atoms make an obvious and significant contribution to the energy band compared with the C atoms. The density of states (DOS) of the C_2B_6 monolayer is calculated in Figure 3C, which further proves that most of the energy level of the C_2B_6 system contributions come from B atoms.

The carrier mobility is further explored, considering the ultra-narrow bandgap of the C_2B_6 monolayer for promising applications in nanodevices. The carrier mobilities of the electrons and holes in transport directions (x and y demonstrated in Figure 1A) are calculated by the Bardeen–Shockley theory demonstrated as Equation 2 (Van de Walle and Martin, 1989):

$$\mu = e\hbar^3 C \Big/ \left(k_B T m^* \sqrt{m_x^* m_y^*}\, D^2 \right), \tag{2}$$

where e is the elementary charge, $\hbar$ represents Planck's constant, and k_B is the Boltzmann constant. The effective mass of the carriers, electrons, and holes is explained by m^*, and the effective mass is obtained using Equation 3:

$$m^* = \hbar^2 \left(\frac{d^2 E_k}{dk^2} \right)^{-1}, \tag{3}$$

where the wave vector is represented by the k. Electronic energy is demonstrated by the E_k. C is the elastic modulus of the C_2B_6 monolayer calculated by $C = [\partial^2 E/\partial((l-l_0)/l_0)^2]/S_0$, where the free energy is E, and the original lattice constant and the difference by the strain are l and l_0, respectively. S_0 is the area of the C_2B_6 monolayer. The energy of the C_2B_6 monolayer under applied uniaxial is demonstrated in Figure 4A. One can see that the sensitivity of energy of the C_2B_6 monolayer to external strain in the y direction is significantly higher than that in the x direction, suggesting the higher elastic modulus of the y direction. Furthermore, D is used to show the potential constant of the C_2B_6 monolayer, which is calculated by $D = \Delta E_{edge}/((l-l_0)/l_0)$, where the ΔE_{edge} is the difference of the band edge by uniaxial strain along the transport directions. As shown in Figure 4B, when the strain is applied in the y direction, the CBM and the VBM can be increased linearly. Meanwhile, the CBM and the VBM of the C_2B_6 monolayer can be decreased linearly by the strain along the x direction, suggesting the external strain is an effective measure to tune the electronic properties of the C_2B_6 monolayer.

The calculated effective mass and deformation potential constant elastic modulus are demonstrated in Table. 1. It is worth noting that the effective mass of the C_2B_6 monolayer along the y direction is as low as 0.406 m*, suggesting higher carrier mobility. The sensitivity of edge energy to strain along x and y directions is similar for electrons and holes. The apparent mechanical anisotropy obtained from the elastic modulus of the C_2B_6 monolayer is calculated as 183 $N{\cdot}m^{-1}$ and 377 $N{\cdot}m^{-1}$, respectively, in the x and y directions. Thus, the pronounced anisotropic carrier mobility of the C_2B_6 monolayer is also obtained such that electrons 360 $cm^2{\cdot}V^{-1}{\cdot}s^{-1}$ and 205 $cm^2{\cdot}V^{-1}{\cdot}s^{-1}$ mobility in the x and y directions, respectively. More importantly, the C_2B_6 monolayer possesses ultrahigh hole mobility in the y direction of approximately 6,342 $cm^2{\cdot}V^{-1}{\cdot}s^{-1}$. The difference of the carrier between the electron and hole in the y direction is also approximately 30 times, suggesting excellent promotion to separate the excited carriers. In addition, the electrons and holes show a

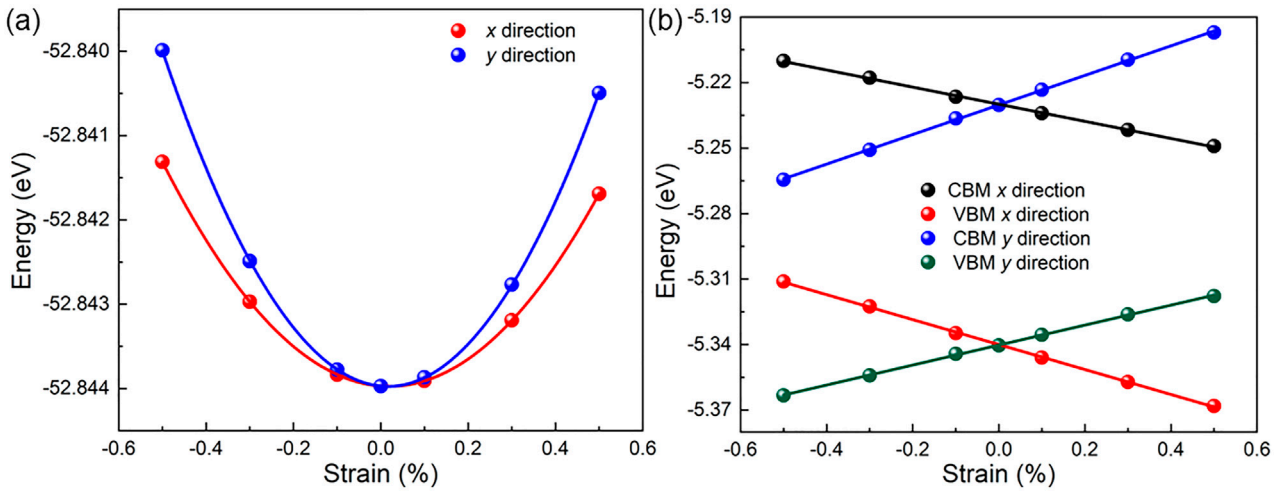

FIGURE 4
Difference of the **(A)** energy and the **(B)** band edge positions of the C_2B_6 monolayer in the *x* and *y* directions.

TABLE 1 Calculated effective mass (*m**), deformation potential constant (*D*, eV), elastic modulus (C, N·m^{-1}), and carrier (electron and hole) mobility (μ, cm^2·V^{-1}·s^{-1}) of the C_2B_6 monolayer along the *x* and *y* directions.

Material (B)	Direction	Carrier	*m**	*D*	*C*	μ
C_2B_6	*x*	Electron	1.221	−1.919	183	360
		Hole	1.743	−2.714		241
	y	Electron	2.121	2.771	377	205
		Hole	0.406	1.574		6,342

favorable transport along the *x* and *y* directions, respectively. The obtained carrier mobility of the C_2B_6 monolayer is even higher than other popular 2D materials, such as the $GaPS_2Se_2$ monolayer (530 cm^2·V^{-1}·s^{-1}) (Zhang Y. et al., 2022), the B_2P_6 monolayer (5,888 cm^2·V^{-1}·s^{-1}) (Ren et al., 2021c), and $MoSi_2N_4$ (2,169 cm^2·V^{-1}·s^{-1}) (Ren et al., 2023b) and is comparable with a Li_2B_6 monolayer (6,800 cm^2·V^{-1}·s^{-1}) (Kai et al., 2018).

The light absorption performance of the C_2B_6 monolayer is further investigated by the absorption coefficient (α), which is calculated by Equation 4 (Zhang L. et al., 2022).

$$\alpha(\omega) = \frac{\sqrt{2}\omega}{c}\left\{\left[\varepsilon_1^2(\omega) + \varepsilon_2^2(\omega)\right]^{1/2} - \varepsilon_1(\omega)\right\}^{1/2}, \quad (4)$$

where the $\varepsilon_1(\omega)$ is the real part of the dielectric constant, and the $\varepsilon_2(\omega)$ is the imaginary part. ω represents the angular frequency, and c is the speed of light in a vacuum. It is worth noting that $\varepsilon_2(\omega)$ can be calculated by Equation 5 (Zhang et al., 2008):

$$\varepsilon_2(q \to O_{\hat{u}}, \hbar\omega) = \frac{2e^2\pi}{\Omega\varepsilon_0}\sum_{k,v,c} \left|\langle \Psi_k^c \left| \hat{u}\cdot r \right| \Psi_k^v \rangle\right|^2 \times \delta(E_k^c - E_k^v - E), \quad (5)$$

where Ψ_k, E_k, and $\hat{u}$ are used to explain the wave function, energy, and unit vector of the electric field of the incident light, respectively. Then, the superscripts (v and c) in the Ψ_k and E_k demonstrate the conduction and valence bands, respectively. Furthermore, $\varepsilon(\omega) = \varepsilon_1(\omega) + i\varepsilon_2(\omega)$ can be used to calculate the complex dielectric function, and the Kramers–Kronig relation can define the real parts ε_1 and ε_2.

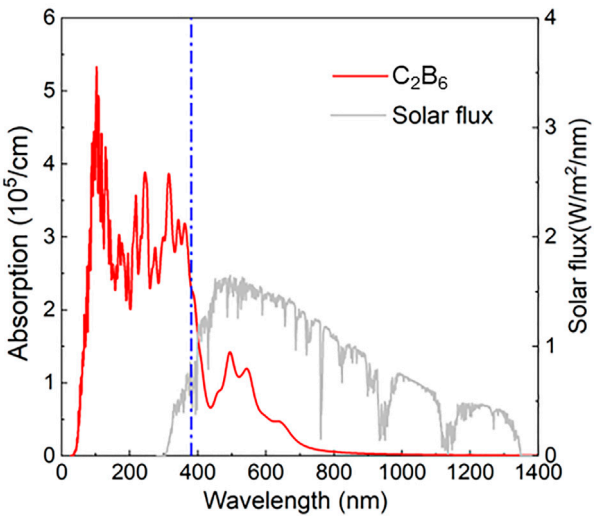

FIGURE 5
Obtained optical absorption spectrum of the C_2B_6 monolayer by the HSE06 method.

The obtained light absorption spectrum of the C_2B_6 monolayer is explained in Figure 5. The C_2B_6 monolayer shows excellent optical

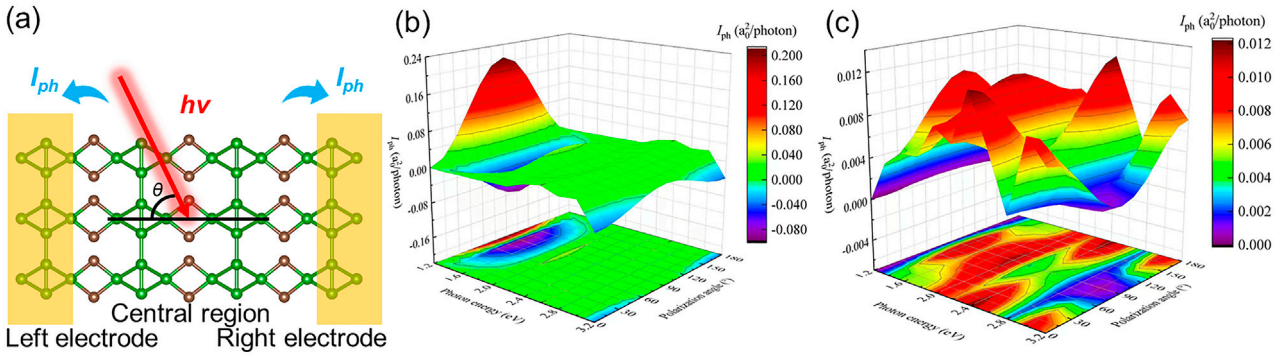

FIGURE 6
(A) Photodetector models and the calculated photocurrent along the **(B)** *x* and **(C)** *y* directions of the C_2B_6 monolayer.

properties in the visible and near-ultraviolet regions with an absorption peak of approximately 3.566 × 10^5 cm^{-1} and a wavelength of approximately 106 nm. The novel absorption coefficient at the visible light range is also obtained at approximately 9.578 × 10^4 cm^{-1} with a wavelength of approximately 450 nm. Such an optical absorption peak of the C_2B_6 monolayer is also higher than other reported 2D materials, such as a CdO/arsenene heterostructure (8.47 × 10^4 cm^{-1}) (Ren et al., 2021d), GaN (4.00 × 10^4 cm^{-1}) (Ren et al., 2020c), and $Mg(OH)_2$ (3.49 × 10^4 cm^{-1}) (Ren et al., 2019).

The excellent carrier mobility and the optical performance of the C_2B_6 monolayer suggest potential applications as a photocurrent device. The model of the C_2B_6 monolayer used as a photocurrent nanodevice is illustrated in Figure 6A with two electrodes. The C and B atoms at the central region are excited by the linearly polarized light in the *z* direction and can induce the photon-generated carriers with the photocurrent flowing to the electrodes as I_{ph}, which can be obtained as Equation 6 (Qin et al., 2024; Li et al., 2024):

$$J_{ph} = \frac{ie}{h}\int \mathrm{Tr}\left\{\Gamma\left[G^{<(ph)} + f(E)\left(G^{>(ph)} - G^{<(ph)}\right)\right]\right\}\mathrm{d}E, \quad (6)$$

where $\Gamma = i(\Sigma_R - \Sigma_L)$ is the coupling of the center area and electrodes in the C_2B_6 monolayer. Σ_L is the interactive self-energy of the left electrode, and the Σ_R is interactive self-energy of the right one. $f(E)$ is the Fermi–Dirac distribution. Green's functions for photon–electron interactions are presented by $G^{>(ph)}$. J_{ph} is normalized by $I_{ph} = J_{ph}/eI_\omega$, and the I_ω demonstrates the photon flux. The calculated unit for the photocurrent is a0 2/photon, where the a_2^0 is used to explain the Boreal radius. The photocurrent is also dependent on the photon energy and polarization angle of the C_2B_6 monolayer; thus, the photocurrent C_2B_6 monolayer is calculated with a different angle and intensity of light incidence in Figure 6B. One can see that the maximal I_{ph} of the C_2B_6 monolayer is approximately 0.24 a_2^0/photon with the energy and the polarization angle of approximately 1.2 eV and 90°, respectively. Note that the anisotropy of carrier mobility also implies different photocurrents in the *x* and *y* directions. The obtained maximal I_{ph} of the C_2B_6 monolayer along the *y* direction is demonstrated in Figure 6C as approximately 0.012 a_2^0/photon at the polarization angle of 90° with the energy of approximately 2.4 eV. The obtained photocurrent of the C_2B_6 is comparable with the other reported 2D materials, for example, MoSSe (0.88 a_2^0/photon) (Cui et al., 2024), $WSe_2/MoSe_2$ (0.65 a_2^0/photon) (Sun et al., 2023) and MoS_2/WSSe (0.71 a_2^0/photon) (Sun et al., 2023) linearly polarized lights.

Furthermore, the dependence of the photocurrent of the C_2B_6 on angle and energy is also different along the *x* and *y* directions compared with Figures 6B, C. The photocurrent of the C_2B_6 can be decreased with increasing energy, and the vertical illumination method can obtain the maximal photocurrent along the *x* direction. Differently, the optimum photocurrent of the C_2B_6 can be induced by the horizontal irradiation method. With increasing energy, there is no unified trend of change for the photocurrent of the C_2B_6 along the *y* direction. Thus, the photocurrent direction can be effectively controlled by adjusting the incident angle, another promising attribute for a photoelectric device. When the C_2B_6 monolayer is illuminated, the photogenerated electrons can move quickly to the conduction band due to the narrow bandgap, inducing the valence band with photogenerated holes. Under the drive of a photocurrent, photogenerated electrons and holes can be rapidly separated due to the strong anisotropy of the mobility, implying that C_2B_6 is a potential high-efficiency photocatalyst.

Conclusion

In summary, a C_2B_6 monolayer is proposed with inherent stability. The puckered crystal structure of the C_2B_6 monolayer presents semiconductor properties with an ultranarrow indirect bandgap of approximately 0.671 eV, while the ultrahigh hole mobility is calculated as 6,342 $cm^2 \cdot V^{-1} \cdot s^{-1}$ in the suitable direction. The calculated anisotropic carrier mobility of the electrons and holes in the C_2B_6 monolayer demonstrates the advantages of carrier separation for use as a photocatalyst. Finally, the excellent light absorption and the photocurrent are also addressed, demonstrating the potential applications for photocatalytic, photovoltaic and optical and cold chain electronic devices.

Data availability statement

The original contributions presented in the study are included in the article/Supplementary Material; further inquiries can be directed to the corresponding authors.

Author contributions

PX: data curation, funding acquisition, and writing–original draft. ZZ: formal analysis, visualization, and writing–review and editing. RZ: data curation, visualization, and writing–review and editing. QS: investigation, supervision, validation, and writing–review and editing. ZM: conceptualization, data curation, project administration, and writing–review and editing. WM: data curation, investigation, supervision and writing–review and editing. ZC: investigation, software, supervision, and writing–review and editing.

Funding

The author(s) declare financial support was received for the research, authorship, and/or publication of this article. The authors thank the Key Research Project of Higher Education Teaching Reform in Jiangsu Province: 2021JSJG160, the Supply-demand Matching Employment and Education Project of the Ministry of Education: 20230107091, the Scientific and Technological Project of Jiangsu Vocational College of Agriculture and Forestry: 2021kj63, and Jiangsu Vocational College of Agriculture and Forestry's 2022 School-level Education and Teaching Reform Research Project: "Design and Operation Teaching Simulation System for Intelligent Cold Chain Logistics Warehousing Center of Agricultural Products" (JSNL2022126).

Conflict of interest

Author QS was employed by Nanjing Boya Intelligent Technology Co., Ltd.

The remaining authors declare that the research was conducted in the absence of any commercial or financial relationships that could be construed as a potential conflict of interest.

Publisher's note

Supplementary material

The Supplementary Material for this article can be found online at: https://www.frontiersin.org/articles/10.3389/fchem.2024.1482006/full#supplementary-material

References

Blöchl, P. E. (1994). Projector augmented-wave method. *Phys. Rev. B* 50, 17953–17979. doi:10.1103/physrevb.50.17953

Cui, Z., Wang, H., Shen, Y., Qin, K., Yuan, P., and Li, E. (2024). $MoSe_2$ and WSSe heterojunction with exceptional power conversion efficiency and photogalvanic effect. *Mater. Today Phys.* 40, 101317. doi:10.1016/j.mtphys.2023.101317

Geim, A. K., and Novoselov, K. S. (2007). The rise of graphene. *Nat. Mater.* 6, 183–191. doi:10.1038/nmat1849

Grest, G., Nagel, S., Rahman, A., and Witten, T., Jr (1981). Density of states and the velocity autocorrelation function derived from quench studies. *J. Chem. Phys.* 74, 3532–3534. doi:10.1063/1.441508

Grimme, S., Antony, J., Ehrlich, S., and Krieg, H. (2010). A consistent and accurate *ab initio* parametrization of density functional dispersion correction (DFT-D) for the 94 elements H-Pu. *J. Chem. Phys.* 132, 154104. doi:10.1063/1.3382344

Haastrup, S., Strange, M., Pandey, M., Deilmann, T., Schmidt, P. S., Hinsche, N. F., et al. (2018). The Computational 2D Materials Database: high-throughput modeling and discovery of atomically thin crystals. *Mater.* 5, 042002. doi:10.1088/2053-1583/aacfc1

Heyd, J., Peralta, J. E., Scuseria, G. E., and Martin, R. L. (2005). Energy band gaps and lattice parameters evaluated with the Heyd-Scuseria-Ernzerhof screened hybrid functional. *J. Chem. Phys.* 123, 174101. doi:10.1063/1.2085170

Heyd, J., Scuseria, G. E., and Ernzerhof, M. (2003). Hybrid functionals based on a screened Coulomb potential. *J. Chem. Phys.* 118, 8207–8215. doi:10.1063/1.1564060

Huang, L., Ren, K., Zhang, G., Wan, J., Zhang, H., Zhang, G., et al. (2024). Tunable thermal conductivity of two-dimensional SiC nanosheets by grain boundaries: implications for the thermo-mechanical sensor. *ACS Appl. Nano Mater.* 7, 15078–15085. doi:10.1021/acsanm.4c01803

Jin, H., Wang, T., Gong, Z. R., Long, C., and Dai, Y. (2018). Prediction of an extremely long exciton lifetime in a Janus-MoSTe monolayer. *Nanoscale* 10, 19310–19315. doi:10.1039/c8nr04568b

Jing, Y., Ma, Y., Li, Y., and Heine, T. (2017). GeP_3: a small indirect band gap 2D crystal with high carrier mobility and strong interlayer quantum confinement. *Nano Lett.* 17, 1833–1838. doi:10.1021/acs.nanolett.6b05143

Kai, R., WenCheng, T., Jian, W., and Hui, L. (2018) "Fatigue reliability Analysis and life bench test of buffer block in car damper," in *2018 IEEE international conference on engineering, Technology and innovation (ICE/ITMC), IEEE*, 1–6.

Kresse, G., and Furthmüller, J. (1996a). Efficiency of ab-initio total energy calculations for metals and semiconductors using a plane-wave basis set. *Comp. Mater. Sci.* 6, 15–50. doi:10.1016/0927-0256(96)00008-0

Kresse, G., and Furthmüller, J. (1996b). Efficient iterative schemes for *ab initio* total-energy calculations using a plane-wave basis set. *Phys. Rev. B* 54, 11169–11186. doi:10.1103/physrevb.54.11169

Kresse, G., and Joubert, D. (1999). From ultrasoft pseudopotentials to the projector augmented-wave method. *Phys. Rev. B* 59, 1758–1775. doi:10.1103/physrevb.59.1758

Li, E., Qin, K., Cui, Z., Shen, Y., Ma, D., Yuan, P., et al. (2024). Electrical properties and current-illumination characteristics of the SiC/GaN lateral heterostructure. *J. Phys. Chem. C* 128, 11827–11834. doi:10.1021/acs.jpcc.4c01809

Lu, N., Zhuo, Z., Guo, H., Wu, P., Fa, W., Wu, X., et al. (2018). CaP3: a new two-dimensional functional material with desirable band gap and ultrahigh carrier mobility. *J. Phys. Chem. Lett.* 9, 1728–1733. doi:10.1021/acs.jpclett.8b00595

Luo, X., Yang, J., Liu, H., Wu, X., Wang, Y., Ma, Y., et al. (2011). Predicting two-dimensional boron-carbon compounds by the global optimization method. *J. Am. Chem. Soc.* 133, 16285–16290. doi:10.1021/ja2072753

Lv, B., Hu, X., Liu, X., Zhang, Z., Song, J., Luo, Z., et al. (2020). Thermal transport properties of novel two-dimensional CSe. *Phys. Chem. Chem. Phys.* 22, 17833–17841. doi:10.1039/d0cp02298e

Miro, P., Audiffred, M., and Heine, T. (2014). An atlas of two-dimensional materials. *Chem. Soc. Rev.* 43, 6537–6554. doi:10.1039/c4cs00102h

Nosé, S. (1984). A unified formulation of the constant temperature molecular dynamics methods. *J. Chem. Phys.* 81, 511–519. doi:10.1063/1.447334

Oganov, A. R., and Glass, C. W. (2006). Crystal structure prediction using *ab initio* evolutionary techniques: principles and applications. *J. Chem. Phys.* 124, 244704. doi:10.1063/1.2210932

Perdew, J. P., Burke, K., and Ernzerhof, M. (1996). Generalized gradient approximation made simple. *Phys. Rev. Lett.* 77, 3865–3868. doi:10.1103/physrevlett.77.3865

Qin, K., Li, E., Shen, Y., Ma, D., Yuan, P., Wang, H., et al. (2024). Hf_2CO_2-based heterojunctions for efficient photocatalytic hydrogen production and highly responsive self-powered flexible photodetector. *Ceram. Int.* doi:10.1016/j.ceramint.2024.08.058

Ren, K., Huo, W., Chen, S., Cheng, Y., Wang, B., and Zhang, G. (2024). High-entropy alloys in thermoelectric application: a selective review. *Chin. Phys. B* 33, 057202. doi:10.1088/1674-1056/ad34c5

Ren, K., Liu, X., Chen, S., Cheng, Y., Tang, W., and Zhang, G. (2020b). Remarkable reduction of interfacial thermal resistance in nanophononic heterostructures. *Adv. Funct. Mater.* 30, 2004003. doi:10.1002/adfm.202004003

Ren, K., Luo, Y., Yu, J., and Tang, W. (2020c). Theoretical prediction of two-dimensional ZnO/GaN van der Waals heterostructure as a photocatalyst for water splitting. *Chem. Phys.* 528, 110539. doi:10.1016/j.chemphys.2019.110539

Ren, K., Ma, X., Liu, X., Xu, Y., Huo, W., Li, W., et al. (2022a). Prediction of 2D IV–VI semiconductors: auxetic materials with direct bandgap and strong optical absorption. *Nanoscale* 14, 8463–8473. doi:10.1039/d2nr00818a

Ren, K., Shu, H., Huang, L., Wang, K., Luo, Y., Huo, W., et al. (2023a). Predicted XN (X = C, Si, Ge, and Sn) monolayers with ultrahigh carrier mobility: potential photocatalysts for water splitting. *J. Phys. Chem. C* 127, 21006–21014. doi:10.1021/acs.jpcc.3c06284

Ren, K., Shu, H., Huo, W., Cui, Z., Yu, J., and Xu, Y. (2021c). Mechanical, electronic and optical properties of a novel B2P6 monolayer: ultrahigh carrier mobility and strong optical absorption. *Phys. Chem. Chem. Phys.* 23, 24915–24921. doi:10.1039/d1cp03838a

Ren, K., Shu, H., Wang, K., and Qin, H. (2023b). Two-dimensional MX_2Y_4 systems: ultrahigh carrier transport and excellent hydrogen evolution reaction performances. *Phys. Chem. Chem. Phys.* 25, 4519–4527. doi:10.1039/d2cp04224j

Ren, K., Wang, K., and Zhang, G. (2022b). Atomic adsorption-controlled magnetic properties of a two-dimensional (2D) Janus monolayer. *ACS Appl. Electron. Mater.* 4, 4507–4513. doi:10.1021/acsaelm.2c00740

Ren, K., Wang, S., Luo, Y., Chou, J.-P., Yu, J., Tang, W., et al. (2020a). High-efficiency photocatalyst for water splitting: a Janus MoSSe/XN (X = Ga, Al) van der Waals heterostructure. *J. Phys. Phys. D. Appl. Phys.* 53, 185504. doi:10.1088/1361-6463/ab71ad

Ren, K., Yan, Y., Zhang, Z., Sun, M., and Schwingenschlögl, U. (2022c). A family of Li_xB_y monolayers with a wide spectrum of potential applications. *Appl. Surf. Sci.* 604, 154317. doi:10.1016/j.apsusc.2022.154317

Ren, K., Yu, J., and Tang, W. (2019). First-principles study of two-dimensional van der Waals heterostructure based on ZnO and $Mg(OH)_2$: A potential photocatalyst for water splitting. *Phys. A* 383, 125916. doi:10.1016/j.physleta.2019.125916

Ren, K., Zheng, R., Lou, J., Yu, J., Sun, Q., and Li, J. (2021a). *Ab initio* calculations for the electronic, interfacial and optical properties of two-dimensional AlN/Zr_2CO_2 heterostructure. *Front. Chem.* 9, 796695. doi:10.3389/fchem.2021.796695

Ren, K., Zheng, R., Yu, J., Sun, Q., and Li, J. (2021b). Band bending mechanism in CdO/arsenene heterostructure: a potential direct Z-scheme photocatalyst. *Front. Chem.* 9, 788813. doi:10.3389/fchem.2021.788813

Ren, K., Zheng, R., Yu, J., Sun, Q., and Li, J. (2021d). Band bending mechanism in CdO/arsenene heterostructure: a potential direct Z-scheme photocatalyst. *Front. Chem.* 9, 788813. doi:10.3389/fchem.2021.788813

Su, H., Wang, W., Shi, R., Tang, H., Sun, L., Wang, L., et al. (2023). Recent advances in quantum dot catalysts for hydrogen evolution: synthesis, characterization, and photocatalytic application. *Carbon Energy* 5, 280. doi:10.1002/cey2.280

Su, H., Yu, X., Wang, W., Wang, L., Tang, H., and Liu, Q. (2022). A 2D bimetallic Ni–Co hydroxide monolayer cocatalyst for boosting photocatalytic H_2 evolution. *Chem. Commun.* 58, 6180–6183. doi:10.1039/d2cc01557a

Sun, L., Wang, W., Kong, T., Jiang, H., Tang, H., and Liu, Q. (2022). Fast charge transfer kinetics in an inorganic–organic S-scheme heterojunction photocatalyst for cooperative hydrogen evolution and furfuryl alcohol upgrading. *J. Mater. Chem. A* 10, 22531–22539. doi:10.1039/d2ta06468e

Sun, M., and Schwingenschlögl, U. (2020a). B2P6: a two-dimensional anisotropic Janus material with potential in photocatalytic water splitting and metal-ion batteries. *Chem. Mater.* 32, 4795–4800. doi:10.1021/acs.chemmater.0c01536

Sun, M., and Schwingenschlögl, U. (2020b). δ-CS: a direct-band-gap semiconductor combining auxeticity, ferroelasticity, and potential for high-efficiency solar cells. *Phys. Rev. Appl.* 14, 044015. doi:10.1103/physrevapplied.14.044015

Sun, M., and Schwingenschlögl, U. (2021). Structure prototype outperforming MXenes in stability and performance in metal-ion batteries: a high throughput study. *Adv. Energy Mater.* 11, 2003633. doi:10.1002/aenm.202003633

Sun, X., Yin, S., Yu, H., Wei, D., Ma, Y., and Dai, X. (2023). A direction-sensitive photodetector based on the two-dimensional $WSe_2/MoSe_2$ lateral heterostructure with enhanced photoresponse. *Results Phys.* 46, 106271. doi:10.1016/j.rinp.2023.106271

Tang, L., Hu, Y., Tang, H., Sun, L., Jiang, H., Wang, W., et al. (2022). Incorporating Ni-polyoxometalate into the S-scheme heterojunction to accelerate charge separation and resist photocorrosion for promoting photocatalytic activity and stability. *J. Phys. Chem. Lett.* 13, 11778–11786. doi:10.1021/acs.jpclett.2c03269

Togo, A., Oba, F., and Tanaka, I. (2008). First-principles calculations of the ferroelastic transition between rutile-type and $CaCl_2$-type SiO_2 at high pressures. *Phys. Rev. B* 78, 134106. doi:10.1103/physrevb.78.134106

Togo, A., and Tanaka, I. (2015). First principles phonon calculations in materials science. *Scr. Mater.* 108, 1–5. doi:10.1016/j.scriptamat.2015.07.021

Van de Walle, C. G., and Martin, R. M. (1989). Absolutedeformation potentials: formulation and *ab initio* calculations for semiconductors. *Phys. Rev. Lett.* 62, 2028–2031. doi:10.1103/physrevlett.62.2028

Wang, J., Li, Y., Deng, L., Wei, N., Weng, Y., Dong, S., et al. (2017). High-performance photothermal conversion of narrow-bandgap Ti_2O_3 nanoparticles. *Adv. Mater* 29, 1603730. doi:10.1002/adma.201603730

Wang, W., Zhang, W., Cai, Y., Wang, Q., Deng, J., Chen, J., et al. (2023). Introducing BN unit boosts photocatalytic H_2O_2 production on metal-free g-C_3N_4 nanosheets. *Nano. Res.* 16, 2177–2184. doi:10.1007/s12274-022-4976-0

Wu, D., Kusada, K., Yamamoto, T., Toriyama, T., Matsumura, S., Gueye, I., et al. (2020). On the electronic structure and hydrogen evolution reaction activity of platinum group metal-based high-entropy-alloy nanoparticles. *Chem. Sci.* 11, 12731–12736. doi:10.1039/d0sc02351e

Yuan, S., Zhou, Q., Wu, Q., Zhang, Y., Chen, Q., Hou, J.-M., et al. (2017). Prediction of a room-temperature eight-coordinate two-dimensional topological insulator: penta-RuS4 monolayer. *npj 2D Mater. Appl.* 1, 29. doi:10.1038/s41699-017-0032-4

Zhang, G., Yu, M.-B., Tung, C.-H., and Lo, G.-Q. (2008). Quantum size effects on dielectric constants and optical absorption of ultrathin silicon films. *IEEE Electron Device Lett.* 29, 1302–1305. doi:10.1109/led.2008.2005651

Zhang, L., Ren, K., Li, J., Cui, Z., and Cheng, H. (2022b). The First-Principles Study of External Strain Tuning the Electronic and Optical Properties of the 2D $MoTe_2/PtS_2$ van der Waals Heterostructure. *Front. Chem.* 10, 934048. doi:10.3389/fchem.2022.934048

Zhang, Y., Liu, X., Wang, Z., Chen, X., Xiao, W., Liu, T., et al. (2022a). The $GaPS_2Se_2$ monolayer: a novel stable 2D Janus semiconductor with anisotropic properties for spontaneous water splitting under the irradiation of solar light. *J. Mater. Chem. C* 10, 17135–17144. doi:10.1039/d2tc03445j

Zhao, L., Huang, L., Wang, K., Mu, W., Wu, Q., Ma, Z., et al. (2024). Mechanical and lattice thermal properties of Si-Ge lateral heterostructures. *Molecules* 29, 3823. doi:10.3390/molecules29163823

Zhao, X., Yang, Y., Hu, Y., Wang, G., Wang, D., Wei, Y., et al. (2023). Theoretical calculation of hydrogen evolution reaction in two-dimensional As_2X_3 (X= S, Se, Te) doped with transition metal atoms. *Appl. Surf. Sci.* 616, 156475. doi:10.1016/j.apsusc.2023.156475